Hierarchical Vector Finite Elements for Analyzing Waveguiding Structures

Seung-Cheol Lee, Jin-Fa Lee, *Member, IEEE*, and Robert Lee, *Senior Member, IEEE*

Abstract—In this paper, we extend the finite-element method into hierarchical higher order bases and the inexact Helmholtz decomposition. With the help of hierarchical basis functions, the approach can adopt well into the p version adaptive process. On the other hand, the inexact Helmholtz decomposition enhances the stability of the finite-element procedure when the operating frequency is low or the element size is very small compared to the wavelength. This approach can also enhance the h version adaptive mesh refinement process since the process may cause very small elements near a singular region. To accomplish the inexact Helmholtz decomposition for the edge elements, the lowest order curl conforming basis functions, the tree–cotree splitting, is utilized, and the general procedure is presented. As a result, a combination of hierarchical higher order basis functions with the inexact Helmholtz decomposition can improve the efficiency and the stability of the hp adaptive mesh refinement process. The accuracy and stability of the proposed approach are also discussed through numerical examples.

Index Terms—Electromagnetic propagation, finite-element method (FEM), higher order basis functions, tree–cotree splitting.

I. INTRODUCTION

THE analysis of two-dimensional waveguiding structures is of significant importance in microwave engineering. It provides impedance information of the transmission lines, the modal configuration of energy propagation, and it is becoming more popular that the two-dimensional eigenanalysis is an integral part of studying real life three-dimensional electromagnetic problems. Various frequency- and time-domain numerical electromagnetic techniques have been presented [1]–[3]; however, it is well accepted that, among them, the finite-element method (FEM) is the most suitable and versatile in handling arbitrary material properties and geometric shapes.

One common approach to improve the accuracy of the FEM analysis is to use higher order basis functions, which can be classified into two families, the *interpolatory* and *hierarchical*. Using interpolatory basis functions [4], the order of the bases needs to be uniform within the computational domain. On the other hand, hierarchical basis functions [5], [6] allow the use of different orders within the same computational domain. This property of the hierarchical elements can be utilized to iteratively increase the order of the basis functions (p refinement) in the regions where an appropriate error estimate is large. Improved accuracy can be also achieved by subdividing a set of elements into another subset of smaller ones of the same order. This process is known as h refinement. An appropriate combination of the above approaches leads to one of the most powerful FEM technologies, the hp adaptive mesh refinement. Therefore, to analyze two-dimensional waveguiding structures, we implement the FEM with higher order bases in a hierarchical way.

However, the popular lowest order curl conforming basis functions are the edge elements [7], and they will suffer low-frequency instability. If the operating frequency becomes very low, the finite-element procedure with the edge elements may converge slowly or break down in iterative solvers. The instability may also occur when the element size is extremely small compared to the wavelength, which can be viewed as a low-frequency situation. To overcome this deficiency, tree–cotree splitting [8] is proposed and implemented. With this technique, the basis vectors are decomposed into two nonoverlapping subspaces, gradient and rotational-like spaces. In solving the vector wave equation, it is of paramount importance to explicitly form basis functions that are pure gradients [5], [6]. Via tree–cotree splitting, our basis functions, are either pure gradient or their complements, rotational-like basis functions. Since the "rotational-like" basis functions are not exactly divergence free, we thus termed the decomposition an "inexact" Helmholtz decomposition. By employing the inexact Helmholtz decomposition, the FEM procedure can be more reliable at low frequencies or in the hp adaptive process.

In this paper, the FEM is enhanced by the hierarchical higher order basis functions and the tree–cotree splitting. Also, the performance of the higher order basis functions are tested through the numerical examples in Section VIII by performing h and p refinements, and the stability of the tree–cotree splitting is verified.

II. FORMULATION

In this study, we employ an $A - V$ formulation from [9] and [10]. For completeness purposes, parts of the formulation are repeated here. The $A - V$ formulation is chosen in this paper since the resultant matrix equation can be better conditioned than the one obtained by E- or H-field formulation [11]. However, instead of utilizing an anisotropic medium, as in [9] and [10], an isotropic case is assumed. For time–harmonic fields in an isotropic medium, Maxwell's equations become

$$\nabla \times \vec{E} = - j\omega\mu_r\mu_0\vec{H}$$
$$\nabla \times \vec{H} = j\omega\varepsilon_r\varepsilon_0\vec{E}$$
$$\nabla \cdot \vec{B} = 0$$
$$\nabla \cdot \vec{D} = 0 \qquad (1)$$

where ε_r and μ_r are the relative permittivity and permeability, respectively. For a waveguiding structure, which is uniform in the z-direction, the electric and magnetic fields can be expressed as

$$\vec{E}(\vec{r};t) = \vec{E}(x,y)e^{-\gamma z}e^{j\omega t}$$
$$\vec{H}(\vec{r};t) = \vec{H}(x,y)e^{-\gamma z}e^{j\omega t} \tag{2}$$

where $\vec{r}$ is a point vector in the waveguide and γ is the propagation constant. The fields can be rewritten in terms of the vector and scalar potentials $\vec{A}$ and φ as

$$\vec{B} = \nabla \times \vec{A}$$
$$\vec{E} = -j\omega\vec{A} - c\nabla\varphi \tag{3}$$

where c denotes the speed of light. By choosing $A_z = 0$ as the gauge condition and applying the splitting $\nabla = \nabla_\tau - \gamma\hat{z}$, Maxwell's equation (1) can be rearranged as

$$\nabla_\tau \times \mu_r^{-1}\nabla_\tau \times \vec{A}_\tau - \gamma^2\mu_r^{-1}\vec{A}_\tau - k_0^2\varepsilon_r\vec{A}_\tau + jk_0\varepsilon_r\nabla_\tau\varphi = 0 \tag{4}$$

$$-\gamma\nabla_\tau \cdot \mu_r^{-1}A_\tau - jk_0\gamma\varepsilon_r\varphi = 0 \tag{5}$$

$$-jk_0\nabla_\tau \cdot \varepsilon_r\vec{A}_\tau - \nabla_\tau \cdot \varepsilon_r\nabla_\tau\varphi - \gamma^2\varepsilon_\tau\varphi = 0 \tag{6}$$

where k_0 is the free-space wavenumber. In the above system of equations, only (4) and (6) are linearly independent, therefore, they are sufficient to describe the boundary value problem (BVP). To ensure a unique solution of the BVP, a set of boundary conditions must be imposed on $\vec{A}$ and φ. In this study, the simplest cases of a perfect electric conductor (PEC) and perfect magnetic conductor (PMC) will be considered as

$$\begin{cases} \vec{n} \times \vec{A}_\tau = 0 \\ \phi = 0 \end{cases} \text{ on PEC} \tag{7}$$

$$\begin{cases} \vec{n} \times \left(\mu_r^{-1}\nabla \times \vec{A}_\tau\right) = 0 \\ (jk_0\vec{A}_\tau + \nabla_\tau\phi) \cdot \vec{n} = 0 \end{cases} \text{ on PMC}. \tag{8}$$

where $\vec{n}$ is the normal vector to the boundary.

III. FINITE-ELEMENT PROCEDURE

Using (4) and (6) and the boundary conditions (7) and (8), the following bilinear form is obtained:

$$B(\vec{v}, \vec{a}) = \int_\Omega \left\{ \mu_r^{-1}(\nabla_\tau \times \vec{v}_\tau) \cdot (\nabla_\tau \times \vec{a}_\tau) - k_0^2\varepsilon_r\vec{v}_\tau \cdot \vec{a}_\tau \right.$$
$$+ \varepsilon_r\nabla_\tau v_z \cdot \nabla_\tau a_z + jk_0\varepsilon_\tau\vec{v}_\tau \cdot \nabla_\tau a_z$$
$$\left. + jk_0\varepsilon_\tau\nabla_\tau v_z \cdot \vec{a}_\tau \right\} d\Omega$$
$$- \gamma^2 \int_\Omega \left\{ \mu_r^{-1}\vec{v}_\tau \cdot \vec{a}_\tau + \varepsilon_r v_z a_z \right\} d\Omega \tag{9}$$

where Ω denotes the domain of interest, $\vec{v}_\tau$ and $\vec{a}_\tau$ are the transverse components of the testing and trial vector potentials in two-dimensional space, and v_z and a_z are the longitudinal components of the testing and trial scalar potentials. To obtain (9),

the standard Galerkin's method and Green's theorems are applied [9], [10]. In the FEM, each state variable is spanned by a set of basis functions. Therefore, the trial function in a sub-domain can be expressed as a linear combination of the basis functions. If $\vec{W}_i^h$ and ϕ_i^h are the vector and scalar basis functions, each trial function will be written as

$$\vec{a}_\tau^h = \sum_{i=0}^{I_\tau} a_{\tau i}^h\vec{W}_i^h \quad a_z^h = \sum_{i=0}^{I_z} a_{zi}^h\phi_i^h \tag{10}$$

where I_τ and I_z denote the numbers of the vector and scalar basis functions, respectively. Since the testing space is the same as the trial space, each testing function can also be expressed as a linear combination of the basis functions. Finally, a generalized eigenmatrix equation is obtained as

$$\sum_{\Omega_e} \begin{pmatrix} [A]_e & jk_0\varepsilon_r[C]_e \\ jk_0\varepsilon_r[C]_e^T & \varepsilon_r[D]_e \end{pmatrix} \begin{bmatrix} \underline{a}_\tau \\ \underline{a}_z \end{bmatrix} = \gamma^2\sum_{\Omega_e} \begin{pmatrix} [B]_e & 0 \\ 0 & [E]_e \end{pmatrix} \begin{bmatrix} \underline{a}_\tau \\ \underline{a}_z \end{bmatrix} \tag{11}$$

where $\underline{a}_\tau$ and $\underline{a}_z$ are the coefficient vectors for the vector and scalar basis functions, respectively, and the sub-matrices used in (11) are given by

$$[A]_e = \int_{\Omega_e} \left\{ \mu_r^{-1}(\nabla \times \vec{W}_i) \cdot (\nabla \times \vec{W}_j) - k_0^2\varepsilon_r\vec{W}_i \cdot \vec{W}_j \right\} d\Omega$$

$$[B]_e = \mu_r^{-1}\int_{\Omega_e} \{\vec{W}_i \cdot \vec{W}_j\} d\Omega$$

$$[C]_e = \int_{\Omega_e} \{\vec{W}_i \cdot \nabla\phi_j\} d\Omega$$

$$[D]_e = \int_{\Omega_e} \{\nabla\phi_i \cdot \nabla\phi_j\} d\Omega$$

$$[E]_e = \varepsilon_r\int_{\Omega_e} \{\phi_i\phi_j\} d\Omega. \tag{12}$$

IV. BASIS FUNCTIONS

In the FEM, the edge elements are widely used as a set of basis functions [7]. However, to obtain a highly accurate result, higher order basis functions may be desired. Furthermore, in performing the hp version adaptive process, hierarchical basis functions will be necessary because they allow each element to have a different order. Therefore, we employ a set of hierarchical higher order basis functions, which is shown in Table I. The vector basis functions of the second and higher order are separated into gradient and rotational-like functions. Table I shows only the rotational-like part of the vector basis functions. The gradient part of the vector basis functions is obtained from the gradients of the second-order and higher order scalar basis functions, which are shown in this same table. The basis functions in Table I are derived mostly following the procedure in [5], except that the rotational-like functions are slightly modified to make the basis functions satisfy the Nedelec criteria [12]. The basis functions in Table I may not be the optimal set for the finite-element bases, and the optimization described in [5] and [6] is not carried out for simplicity. However, they will provide,

TABLE I
HIERARCHICAL VECTOR AND SCALAR BASIS FUNCTIONS

Order	Whitney/Rotational-like functions	Number of the functions	Scalar functions	Number of the functions
1	$\varsigma_i \nabla \varsigma_j - \varsigma_j \nabla \varsigma_i$	3	ς_i	3
2	$-2\varsigma_i \varsigma_j \nabla \varsigma_k + \varsigma_j \varsigma_k \nabla \varsigma_i + \varsigma_k \varsigma_i \nabla \varsigma_j$	2	$\varsigma_i \varsigma_j$	3
3	$\varsigma_i \varsigma_j (\varsigma_j \nabla \varsigma_k - \varsigma_k \nabla \varsigma_j)$	3	$\varsigma_i \varsigma_j (\varsigma_i - \varsigma_j)$	3
			$\varsigma_i \varsigma_j \varsigma_k$	1
4	$\varsigma_i \varsigma_j (\varsigma_i - \varsigma_j)(\varsigma_j \nabla \varsigma_k - \varsigma_k \nabla \varsigma_j)$	3	$\varsigma_i \varsigma_j (\varsigma_i - \varsigma_j)^2$	3
	$\varsigma_i \varsigma_j \varsigma_k ((\varsigma_i - \varsigma_j) \nabla \varsigma_k + (\varsigma_j - \varsigma_k) \nabla \varsigma_i + (\varsigma_k - \varsigma_i) \nabla \varsigma_j)$	1	$(\varsigma_i \varsigma_j \varsigma_k)(\varsigma_i - \varsigma_j)$	2
5	$\varsigma_i \varsigma_j (\varsigma_i - \varsigma_j)^2 (\varsigma_j \nabla \varsigma_k - \varsigma_k \nabla \varsigma_j)$	3	$\varsigma_i \varsigma_j (\varsigma_i - \varsigma_j)^3$	3
	$\varsigma_i \varsigma_j \varsigma_k (-2\varsigma_i \varsigma_j \nabla \varsigma_k + \varsigma_j \varsigma_k \nabla \varsigma_i + \varsigma_k \varsigma_i \nabla \varsigma_j)$	2	$(\varsigma_i \varsigma_j \varsigma_k)(\varsigma_i \varsigma_j)$	3

at least, the general performance that any set of hierarchical higher order basis functions should produce. One advantage of the basis functions in Table I is that the inexact Helmholtz decomposition is already fulfilled for the higher order vector basis functions. However, the edge elements, the first-order vector basis functions, are not yet decomposed, and a possible way is presented in Section V.

V. TREE–COTREE SPLITTING

A major disadvantage of the edge elements is that they may be unreliable for low frequencies [11]. Furthermore, the same deficiency can take place when the element size becomes much smaller than the wavelength. This situation can be crucial in performing the h version adaptive process. In the h-adaptive process, the element size can be extremely small near singularities. To remedy this problem, we employ the tree–cotree splitting [13] to accomplish the inexact Helmholtz decomposition for the edge elements.

A minimum spanning tree in a finite-element mesh can be found by applying a graph theory since a mesh of finite elements is also a graph. The edges on the tree are termed tree edges, while the remaining ones are called cotree edges. Before describing the algorithm for the tree–cotree splitting, it would be convenient to define the following notations:

V_i — ith node;
$\{i, j\}$ — edge formed by nodes i and j;
$N(i)$ — Set of all the nodes that are connected to node i;
$B(i)$, $B(\{i, j\})$ — boundary condition of node i, and edge $\{i, j\}$, respectively;
$ID(i)$ — ID number of node i;
M_i — Mark flag of node i.

In using the inexact Helmholtz splitting, all the nodes on the perfect conductor need to be held at the same potential, therefore, they will have the same number. Therefore, it would be necessary to start by establishing the algorithm for node numbering.

```
Algorithm 1: Node numbering
1) For every node i, set
   ID(i) = NOT_NUMBERED
2) set numG = −1
3) Find a node V_i, such that
    a. B(i) == PEC and
    b. ID(i) == NOT_NUMBERED
```
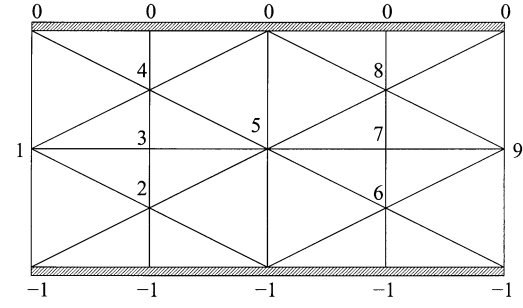

Fig. 1. Node numbering of a two-dimensional mesh graph.

```
4) Does such a V_i exist? If NO goto step
   11
5) set ID(i) = numG
6) add node V_i to set F
7) Is set F empty? If YES goto step 3
8) set V_j  =  Last entry of F, and remove V_j
   from F
9) For every node V_k ∈ N(j), if ID(k) ==
   NOT_NUMBERED and B({j,k}) == PEC then
       a. set ID(k) = numG, and
       b. add V_k to F
10) goto step 7
11) Is numG == −1? If NO goto step 13
12) Pick a node V_i such that ID(i)      ==
    NOT_NUMBERED, and set ID(i)  =  numG,
    increment numG by 1
13) for every node V_i, if
    ID(i)          ==          NOT_NUMBERED, set
    ID(i) = numG and increment numG by 1
```

A sample result of applying Algorithm 1 is shown in Fig. 1. The PEC, which is marked as −1, is assumed to be grounded. After numbering nodes, the next step will be marking the tree and cotree edges.

```
Algorithm 2: Tree-cotree splitting of mesh
graph
1) for every edge {i,j}, reset M({i,j})      =
   CO_TREE
2) for every node V_i, reset
   M(i) = NOT_DONE
3) for every node V_i, if ID(i) == −1 add V_i
   to F
4) Is F empty? If YES then END the proce-
   dure
5) set V_i = first entry of F and remove V_i from
   F
6) for every node V_j ∈ N(i) if ID(j) >= 0 and
   M(j) = NOT_DONE then
       a. M({i,j}) = TREE, and
       b. M(j) = DONE, and
       c. Add V_j to F
7) goto step 4
```
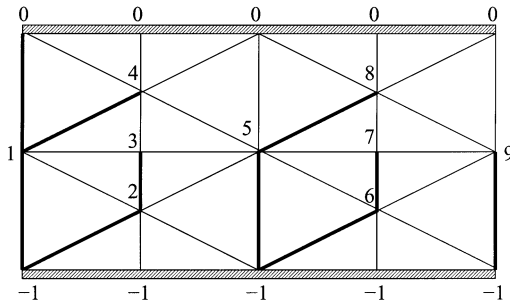
Fig. 2.   Tree–cotree splitting of mesh graph.

A sample result using Algorithm 2 is shown in Fig. 2. The bold-lined edges are the tree edges. In Fig. 2, the number of tree edges is ten, which is exactly the same as the number of unknowns that we numbered in Algorithm 1. Namely, at this moment, we can replace the edge-element basis functions on tree edges with the pure gradient basis functions on the vertex nodes. Note that, in applying Algorithm 2, we have lumped all the physical nodes on the same PEC into one node.

After finding a tree, the edge elements on the tree edges are replaced by $\nabla \varsigma_i$, where ς_i is the bary-centric function on node i. In doing so, the degrees of freedom for tree edges are removed and a new set of unknowns assigned on vertices is added. Since ς_i is a continuous function, the tangential field continuity for $\nabla \varsigma_i$ is maintained. With this modification, the vector basis functions are completely separated into two groups: gradient functions and rotational-like functions. As a result, the tree–cotree splitting and (11) result in the following generalized eigenmatrix equation:

$$\sum_{\Omega_e} \begin{pmatrix} -k_0^2 \varepsilon_r [D_{GG}]_e & -k_0^2 \varepsilon_r [C_{RG}]_e^T & jk_0 \varepsilon_r [D_{GS}]_e \\ -k_0^2 \varepsilon_r [C_{RG}]_e & [A']_e & jk_0 \varepsilon_r [C_{RS}]_e \\ jk_0 \varepsilon_r [D_{GS}]_e^T & jk_0 \varepsilon_r [C_{RS}]_e^T & \varepsilon_r [D]_e \end{pmatrix} \begin{bmatrix} \underline{a}_{\tau G} \\ \underline{a}_{\tau R} \\ \underline{a}_z \end{bmatrix}$$
$$= \gamma^2 \sum_{\Omega_e} \begin{pmatrix} \mu_r^{-1} [D_{GG}]_e & \mu_r^{-1} [C_{GR}]_e^T & 0 \\ \mu_r^{-1} [C_{RG}]_e & [B']_e & 0 \\ 0 & 0 & [E]_e \end{pmatrix} \begin{bmatrix} \underline{a}_{\tau G} \\ \underline{a}_{\tau R} \\ \underline{a}_z \end{bmatrix} \tag{13}$$

where $[A']_e$ and $[B']_e$ are the same operations with $[A]_e$ and $[B]_e$, but with only the rotational-like functions, and $\underline{a}_{\tau G}$ and $\underline{a}_{\tau R}$ are the coefficient vectors for the gradient and rotational-like functions, respectively. The other sub-matrices are

$$[C_{RG}]_e = \int_{\Omega_e} \{ \vec{W}_{Ri} \cdot \vec{W}_{Gj} \} d\Omega \tag{14}$$

$$[C_{RS}]_e = \int_{\Omega_e} \{ \vec{W}_{Ri} \cdot \nabla \phi_j \} d\Omega \tag{15}$$

$$[D_{GG}]_e = \int_{\Omega_e} \{ \vec{W}_{Gi} \cdot \vec{W}_{Gj} \} d\Omega \tag{16}$$

$$[D_{GS}]_e = \int_{\Omega_e} \{ \vec{W}_{Gi} \cdot \nabla \phi_j \} d\Omega \tag{17}$$

where $\vec{W}_G$ and $\vec{W}_R$ are the gradient and rotational-like functions, respectively. From the fact that $\vec{W}_G$ are the gradients of

scalar basis functions, it can be observed that most of the entries of $[C_{RG}]_e$ and $[C_{RS}]_e$ are the same. In particular, when the problem domain contains exactly one PEC body, the matrices $[C_{RG}]_e$ and $[C_{RS}]_e$ are exactly the same. The same situation holds for the matrices $[D_{GG}]_e$, $[D_{GS}]_e$, and $[D]_e$.

To obtain the dominant modes in a waveguide, we need to find the smallest eigenvalues of (13). However, the Lanczos algorithm, which is employed in this study, computes the largest eigenvalues much faster than the smallest ones in most cases [10]. Thus, for better convergence, (13) needs to be modified so that the dominant modes are represented by the largest eigenvalues from the modified equation, as described in [10].

VI. CONSTRUCTION OF MATRICES

For the efficient construction of (13), we employ a so-called universal matrix approach, which was introduced in [14]. In [5] and [15], explicit ways of building the universal matrices for tetrahedral elements of arbitrary order and triangular elements for the lowest order are shown, respectively. A similar procedure can be applied for triangular elements of arbitrary order. Following the steps in [5], the universal matrices for triangular elements of arbitrary order can also be obtained. Any vector basis function can be expressed as

$$\vec{W}_i = \sum_{m=1}^{2} N_{im}(\varsigma_1, \varsigma_2) \nabla \varsigma_m \tag{18}$$

where $N_{im}(\varsigma_1, \varsigma_2)$ is a scalar function composed of ς_1 and ς_2. In (18), ς_3 has been removed by $\varsigma_3 = 1 - \varsigma_1 - \varsigma_2$. Therefore,

$$\int_{\Omega_e} \{ \vec{W}_i \cdot \vec{W}_j \} d\Omega_e = \Delta \sum_{m=1}^{2} \sum_{n=1}^{2} \nabla \varsigma_m \cdot \nabla \varsigma_n T_{ij}^{mn} \tag{19}$$

where Δ is the area of the triangle, and T_{ij}^{mn} can be written as

$$T_{ij}^{mn} = 2 \int_{\varsigma_2=0}^{1} \int_{\varsigma_1=0}^{1-\varsigma_2} N_{im}(\varsigma_1, \varsigma_2) N_{jn}(\varsigma_1, \varsigma_2) d\varsigma_1 d\varsigma_2. \tag{20}$$

Also, by taking the curl of (18),

$$\nabla \times \vec{W}_i = \left(\frac{\partial N_{i2}(\varsigma_1, \varsigma_2)}{\partial \varsigma_1} - \frac{\partial N_{i1}(\varsigma_1, \varsigma_2)}{\partial \varsigma_2} \right) \nabla \varsigma_1 \times \nabla \varsigma_2. \tag{21}$$

Therefore,

$$\int_{\Omega_e} \{ \nabla \times \vec{W}_i \cdot \nabla \times \vec{W}_j \} d\Omega_e = \Delta (\nabla \varsigma_1 \times \nabla \varsigma_2)(\nabla \varsigma_1 \times \nabla \varsigma_2) S_{ij} \tag{22}$$

where S_{ij} is

$$S_{ij} = 2 \int_{\varsigma_2=0}^{1} \int_{\varsigma_1=0}^{1-\varsigma_2} \left(\frac{\partial N_{i2}(\varsigma_1, \varsigma_2)}{\partial \varsigma_1} - \frac{\partial N_{i1}(\varsigma_1, \varsigma_2)}{\partial \varsigma_2} \right)$$
$$\times \left(\frac{\partial N_{j2}(\varsigma_1, \varsigma_2)}{\partial \varsigma_1} - \frac{\partial N_{j1}(\varsigma_1, \varsigma_2)}{\partial \varsigma_2} \right) d\varsigma_1 d\varsigma_2. \tag{23}$$

Moreover, it can be shown that

$$(\nabla \varsigma_i \times \nabla \varsigma_j) \cdot (\nabla \varsigma_i \times \nabla \varsigma_j) = \frac{1}{4\Delta^2}. \quad (24)$$

Therefore, (22) can be more simply written as

$$\int_{\Omega_e} \left\{ \nabla \times \vec{W}_i \cdot \nabla \times \vec{W}_j \right\} d\Omega_e = \frac{1}{4\Delta} S_{ij}. \quad (25)$$

For the scalar basis functions, it can be shown that

$$\int_{\Omega_e} \{\phi_i \phi_j\} d\Omega_e = \Delta M_{ij} \quad (26)$$

where M_{ij} is found using a similar procedure as T_{ij}^{mn} and S_{ij}. It can be easily seen that the three expressions (19), (25), and (26) are sufficient for constructing the matrix (13). Once the universal matrices are obtained, the right-hand side of (26) can be used for local matrix construction, which is obviously less expensive and more accurate than numerical integration. Also, it can be easily observed that this approach is beneficial, especially for higher order basis functions.

VII. CONSTRAINT EQUATION

It is indicated in [10] that, while solving (13), nonphysical modes, trivial solutions, may occur. Although they can be easily identified, their occurrence may degrade numerical efficiency and stability of the eigensolver. Therefore, it is desirable to eliminate those nonphysical modes. To constrain the nonphysical modes, a constrained Lanczos algorithm is introduced in [10], in which a constraint equation is used to suppress the trivial solutions completely. To set up the constraint equation, we start by identifying the trivial solution space V_{NULL}^h

$$V_{\text{NULL}}^h = \left\{ \begin{bmatrix} \vec{v}_\tau \\ v_z \end{bmatrix} : \vec{v}_\tau = G v_z = \frac{j}{k_0} \nabla_\tau v_z \right\} \quad (27)$$

where G is a gradient operator scaled by j/k_0. Note that any vector in V_{NULL}^h produces a nonphysical mode. By the tree–cotree splitting, $\vec{v}_\tau$ can be separated into a gradient and a rotational-like parts, and (27) becomes

$$V_{\text{NULL}}^h = \left\{ \begin{bmatrix} \vec{v}_{\tau G} \\ \vec{v}_{\tau R} \\ v_z \end{bmatrix} : \begin{bmatrix} \vec{v}_{\tau G} \\ \vec{v}_{\tau R} \end{bmatrix} = \begin{bmatrix} G \\ 0 \end{bmatrix} v_z \right\}. \quad (28)$$

where $\vec{v}_{\tau G}$ is a gradient vector function, and $\vec{v}_{\tau R}$ is a rotational-like vector function. In the FEM, G can be written as a matrix form $[G]$, and it can be easily found from the fact that the gradient vector basis functions are the gradients of scalar basis functions. Especially when the number of PEC bodies is one, the following equation can be derived from (27):

$$[G] = \frac{j}{k_0} [I] \quad (29)$$

where $[I]$ is the identity matrix. If the number of PECs is more than one, a number of zero row vectors need to be added in (29), and one zero column vector for the non-PEC case. Using the orthonomality of the physical (nonspurious) modes in the

waveguide, the constraint equation can be obtained. Equation (11) can be written as

$$\mathbf{A}\underline{a}_i = \lambda_i \mathbf{B}\underline{a}_i \quad (30)$$

where $\underline{a}_i$ and λ_i are the ith eigenpair. Similarly, another equation can be obtained for the jth eigenpair as

$$\mathbf{A}\underline{a}_j = \lambda_j \mathbf{B}\underline{a}_j. \quad (31)$$

Postmultiplying (30) by $\underline{a}_j^T$ and (31) by $\underline{a}_i^T$, and then subtracting leads to

$$(\lambda_i - \lambda_j)\underline{a}_i \mathbf{B}\underline{a}_j = 0 \quad (32)$$

where the symmetry of $\mathbf{A}$ and $\mathbf{B}$ was utilized. From (32), it follows that

$$\underline{a}_i^T \mathbf{B}\underline{a}_j = \delta_{ij} \quad (33)$$

where δ_{ij} is the Kronecker delta function. Expanding (33) leads to

$$\int_\Omega \left\{ \mu_r^{-1} \vec{a}_\tau^i \cdot \vec{a}_\tau^j + \varepsilon_r a_z^i a_z^j \right\} d\Omega = \delta_{ij}. \quad (34)$$

Taking into account that $\vec{a}_\tau$ is separated into gradient and rotational-like functions by the tree–cotree splitting

$$\vec{a}_\tau = \vec{a}_{\tau G} + \vec{a}_{\tau R} \quad (35)$$

(34) is rearranged as

$$\int_\Omega \left\{ \mu_r^{-1} \left(\vec{a}_{\tau G}^i + \vec{a}_{\tau R}^i \right) \cdot \left(\vec{a}_{\tau G}^j + \vec{a}_{\tau R}^j \right) + \varepsilon_r a_z^i a_z^j \right\} d\Omega = \delta_{ij}. \quad (36)$$

Since a physical solution $\vec{a}^j$ needs to be orthogonal to any trivial solution $\vec{a}^i \in V_{\text{NULL}}^h$, the constraint equation for the physical solution can be obtained from (28) and (36) as

$$\begin{bmatrix} \underline{v}_z^T G^T & 0 & \underline{v}_z^T \end{bmatrix} \begin{bmatrix} \mu_r^{-1}[D_{GG}]_e & \mu_r^{-1}[C_{GR}]_e & 0 \\ \mu_r^{-1}[C_{GR}]_e^T & \mu_r^{-1}[B']_e & 0 \\ 0 & 0 & [E]_e \end{bmatrix} \begin{bmatrix} \underline{a}_{\tau G} \\ \underline{a}_{\tau R} \\ \underline{a}_z \end{bmatrix} = 0$$

$$\Rightarrow \begin{bmatrix} G^T & 0 & I \end{bmatrix} \begin{bmatrix} \mu_r^{-1}[D_{GG}]_e & \mu_r^{-1}[C_{GR}]_e & 0 \\ \mu_r^{-1}[C_{GR}]_e^T & \mu_r^{-1}[B']_e & 0 \\ 0 & 0 & [E]_e \end{bmatrix} \begin{bmatrix} \underline{a}_{\tau G} \\ \underline{a}_{\tau R} \\ \underline{a}_z \end{bmatrix} = 0. \quad (37)$$

If (37) is imposed in the Lanczos algorithm, as shown in [10], the nonphysical modes are constrained since they do not satisfy (37).

VIII. NUMERICAL RESULTS

To test the basis functions applied in this study, h and p refinements using uniform meshes and uniform order of the basis functions were carried out. Also, the stability of the tree–cotree splitting was investigated by reducing the size of the elements in each refinement step.

A. Convergence Study

To check the accuracy of the higher order basis functions, a simple rectangular waveguide was analyzed. Although our
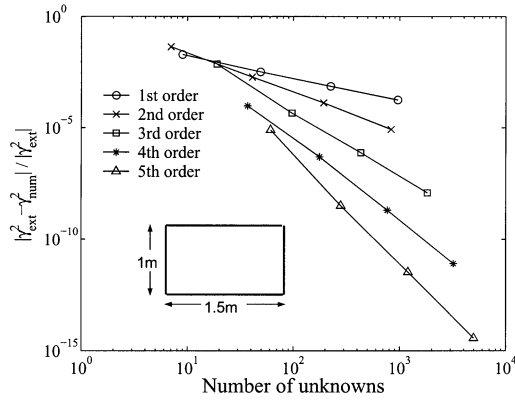
Fig. 3. h-version refinement to obtain the TE_{10} mode in a rectangular waveguide.

Fig. 4. p-version refinement to obtain the TE_{10} mode in a rectangular waveguide.

FEM implementation is capable of analyzing arbitrarily shaped waveguides, we simulated the simplest structure in order to easily compare our approach to the exact solutions. The first example is a convergence test for various orders. For this test, each element was divided into four elements at a step, and the errors of the propagation constants were obtained at each step. For example, the propagation constants were calculated with two elements at the first step, and then with eight elements, 32 elements, and so on. By discretizing the geometry finer, the h refinement behavior can be observed. 1.5 m × 1 m air-filled rectangular waveguide was used in this test, and the frequency was set to 200 MHz. The error is defined by $|\gamma_{\mathrm{ext}}^2 - \gamma_{\mathrm{num}}^2|/|\gamma_{\mathrm{ext}}^2|$, where γ_{ext}^2 is the square of the exact propagation constant obtained from the analytical solution and γ_{num}^2 is the square of the approximate propagation constant obtained from our approach. Since the fields are smooth in this problem, the convergence rates can be predicted theoretically by

$$\left|\gamma_{\mathrm{ext}}^2 - \gamma_{\mathrm{num}}^2\right| \propto \left\|\vec{E}_{\mathrm{ext}} - \vec{E}_{\mathrm{num}}\right\|^2 \propto h^{2p} \propto N^{-p} \qquad (38)$$

where $\vec{E}_{\mathrm{ext}}$ and $\vec{E}_{\mathrm{num}}$ are the exact and numerical values of the $\vec{E}$-field, respectively, h is the typical element size, N is the number of unknowns, and p is the order of the basis functions [16]. Equation (38) is generally valid provided that the solution $\vec{E}$ meets smoothness requirements and $h < 1$. For this numerical experiment, as well as all the following ones, an 800-MHz CPU and 256-MB RAM LINUX PC was used. The errors of the numerical solutions for the TE_{10} mode, the first dominant mode, are plotted in Fig. 3, and the convergence behavior is as expected by (38). In this situation, raising the order of the basis functions while keeping the number of elements the same, which is the p refinement, would be a better choice. The convergence characteristics of the p refinement are shown in Fig. 4. As the order of the basis functions is increased, the rate of convergence generally gets higher. Compared to the convergence rate of the h refinement, that of the p refinement is much higher in this problem. Also, it is shown in Fig. 5 that much less time would be taken with the higher order basis functions to obtain a certain degree of accuracy. Therefore, at least in this specific problem, performing p refinement would be a better choice.
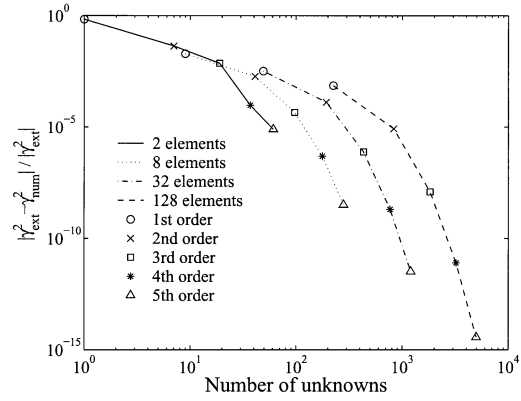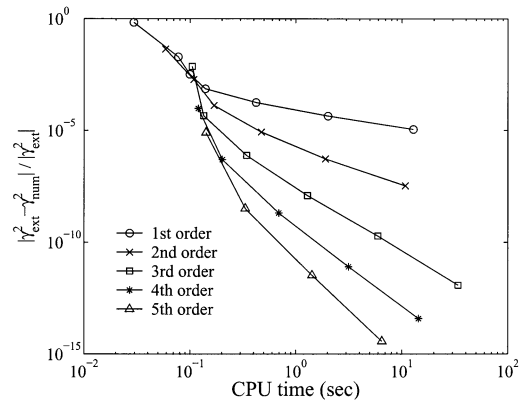

Fig. 5. h refinement versus CPU time of a rectangular waveguide.

However, if it is considered that the fields are smooth inside the simple rectangular waveguide, to carry out the same experiments for the geometry containing singularities would be necessary. The cross section of a shielded microstrip line, shown in Fig. 6, contains singularities inside, and it may cause inaccuracy in the numerical analysis. In this problem, it is shown in [17] that for the region near the singular point

$$\vec{E} \propto \rho^{-0.5} \qquad (39)$$

where ρ is the distance from the singular point. Since $\rho^{-0.5}$ cannot be well expressed by the interpolation polynomials, the numerical error for the electric field will be

$$\vec{E}_{\mathrm{ext}} - \vec{E}_{\mathrm{num}} \propto \rho^{-0.5}. \qquad (40)$$

Therefore,

$$\left\|\vec{E}_{\mathrm{ext}} - \vec{E}_{\mathrm{num}}\right\|^2 \propto \int_0^{2\pi}\int_0^h \left(\rho^{-0.5}\right)^2 \rho \, d\rho \, d\phi \propto h \propto N^{-0.5}. \qquad (41)$$

It can be shown that the asymptotic convergence rate for singular solutions depends only on the intensity of the singularity and not on the order of the polynomial interpolation [16]. It can be noticed from (41) that the convergence rates for the h refinement will not be enhanced by raising the order of the basis functions. In this example, the numerical experiment was carried out for the frequency of 1 GHz. Since there is no analytical solution
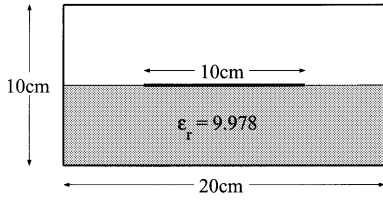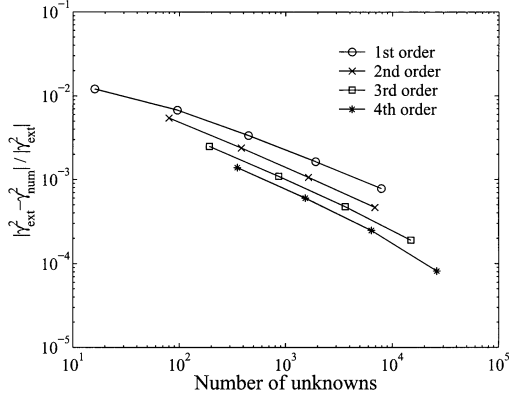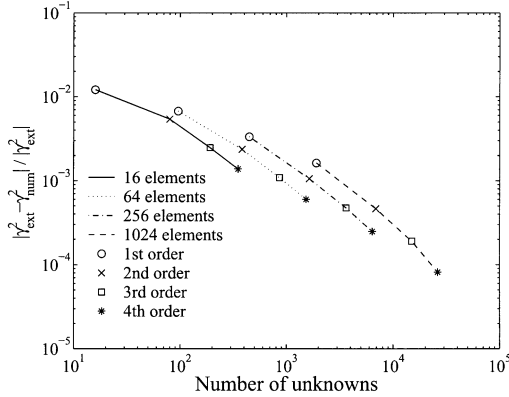
Fig. 6. Geometry of a shielded microstrip line.

Fig. 7. *h*-version refinement to obtain a quasi-TEM mode in a shielded microstrip line.

Fig. 8. *p*-version refinement to obtain a quasi-TEM mode in a shielded microstrip line.

Fig. 9. *h* refinement versus CPU time of a shielded microstrip line.

Fig. 10. Geometry of a partially filled waveguide.

Fig. 11. *h*-version refinement to obtain the first mode in a partially filled waveguide.

available for the shielded microstrip line, we obtained the propagation constant of the quasi-TEM mode with fourth-order basis functions and 4096 elements, and used the result as the reference value. The h and p refinements were carried out in the same way as the previous waveguide problem, and the results are given in Figs. 7 and 8. The rate of convergence is much lower for both the h and p versions than for the rectangular waveguide problem. The slopes in Fig. 7 are $-0.48 \sim -0.58$, and they are in agreement with the expected result from (41). The convergence rates of the p refinement in Fig. 8 are almost constant and twice those of the h refinement, which is consistent with the electrostatic problem [16]. The efficiency of the FEM is slightly enhanced by the higher order basis functions, as shown in Fig. 9.

A similar example is a partially filled waveguide problem, as shown in Fig. 10. The singularities for the electric field occur at the 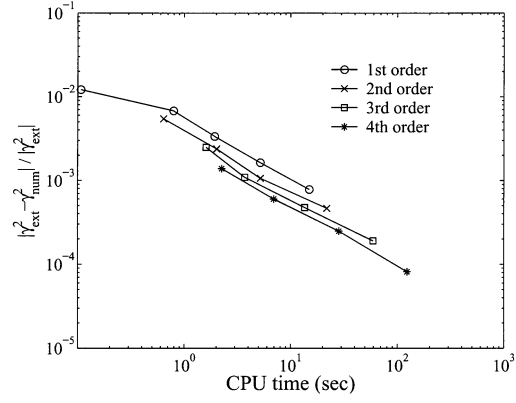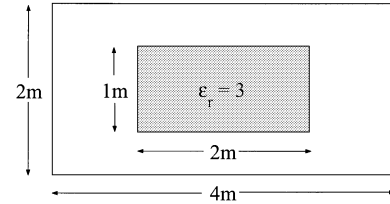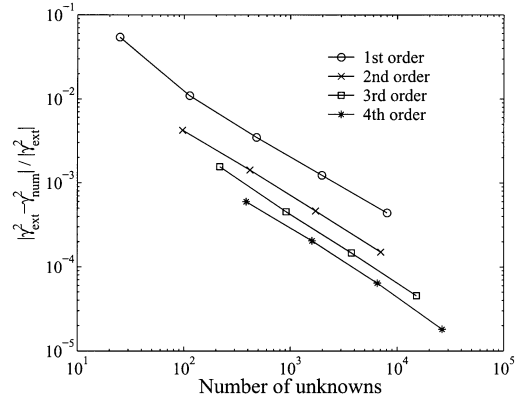corners of the dielectric region, and the order of the singularity is found from [17, eq. (4.66)]. Thus, the electric field near a corner varies as

$$\vec{E} \propto \rho^{-0.16}. \tag{42}$$

Following the procedure of (40) and (41), one can obtain

$$\left\| \vec{E}_{\text{ext}} - \vec{E}_{\text{num}} \right\|^2 \propto h^{1.68} \propto N^{-0.84}. \tag{43}$$

For the numerical experiments, the frequency was set to 70 MHz, and Fig. 11–13 are the results of the experiments. Those results are in agreement with the ones predicted by (43). Since the singularity of this example is weaker, the convergence rates for all cases are better than those of the shielded microstrip-line problem. However, the presence of the singularity results in a uniform convergence rate regardless of the order of the basis functions.

For the problems that include singularity, the accuracy of the FEM solution is determined by the intensity of the singularity.
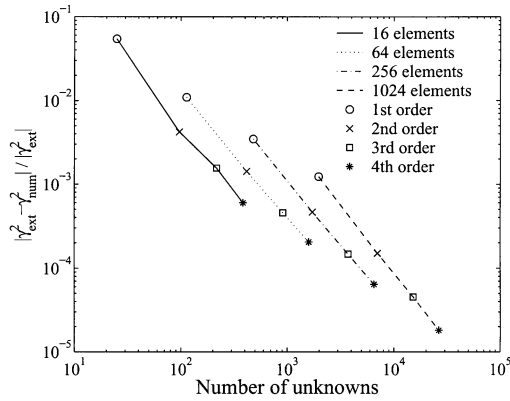
Fig. 12.　p-version refinement to obtain the first mode in a partially filled waveguide.
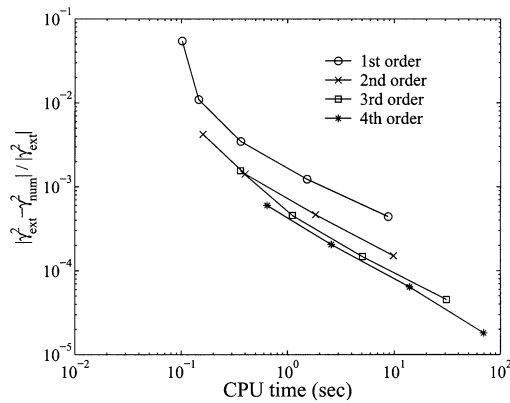

Fig. 14.　Iteration counts for the TE_{10} mode in a waveguide by the Lanczos algorithm—first-order basis functions.

Fig. 13.　h refinement versus CPU time of a partially filled waveguide.

Fig. 15.　Iteration counts for the TE_{10} mode in a waveguide by the Lanczos algorithm—third-order basis functions.

Even the edge elements are affected by the singularity, and exhibit a lower convergence rate than that of a smooth solution. Although the p refinement still performs better than the h refinement, the convergence rate is still very low. A possible way to achieve a better convergence rate and efficiency is to utilize hp adaptive refinement. Namely, small-sized elements are used for regions containing singularities and higher order basis functions are used for regions where the fields are smooth. A similar analysis for electrostatic problems is presented in [16], and it is shown that a nonuniform h refinement combined with higher order basis functions is able to achieve a much better convergence rate for the problems of singularities.

B. Stability of the Tree–Cotree Splitting

To indicate the advantages of using the tree–cotree splitting over the conventional edge elements, the geometry of the rectangular waveguide was discretized several times, and the number of iterations was obtained at each step. The size of each element can be extremely small after several steps, and the benefit of the tree–cotree splitting can be easily seen in this situation. For this example, 15 cm × 10 cm rectangular waveguide was analyzed and the frequency was set to 10 MHz. In Figs. 14 and 15, the number of iterations for finding the TE_{10} mode in the Lanczos algorithm is presented. In our Lanczos solver, the iteration stops when the residual is less than 10^{-10}. It can be clearly
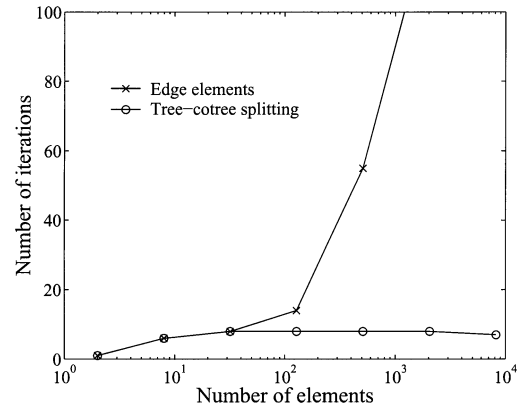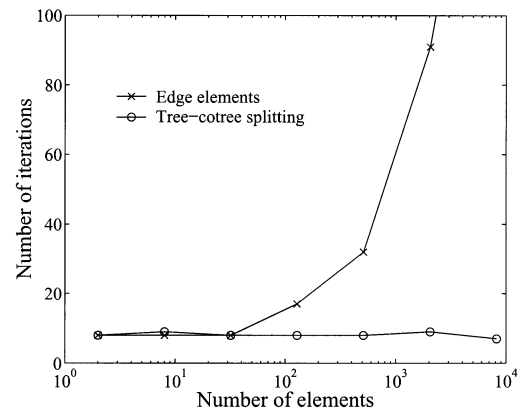
seen that the edge elements are affected by the size of the element, whereas when the tree–cotree splitting is applied, the convergence behavior is very stable for any size of the elements, which can be a great advantage in the h version of adaptive refinement.

IX. CONCLUSIONS

In this paper, a generalized eigenmatrix equation in terms of the higher order basis functions and tree–cotree splitting have been derived. Also, an efficient matrix assembly and the constraint equation that prevents the occurrence of the spurious modes have been discussed. The numerical results have verified the advantages of the higher order basis functions and tree–cotree splitting. However, the accuracy and efficiency of the higher order basis functions were dependent on the problem. For nonsmooth solutions, uniform refinements converged slowly to the exact solutions regardless of the basis order, thus, the adaptive refinement technique was suggested. It was also verified that the tree–cotree splitting might enhance the stability of the finite-element procedure.

Columbus, for his useful discussions about the singularity issues and helping in the preparation of this paper's manuscript.

References

[1] E. Schwig and W. B. Bridges, "Computer analysis of dielectric waveguides: a finite difference method," *IEEE Trans. Microwave Theory Tech.*, vol. MTT-32, pp. 531–541, May 1984.

[2] T. Q. Ho and B. Beker, "Frequency-dependent characteristic of shielded broadside coupled microstrip lines on anisotropic substrate," *IEEE Trans. Microwave Theory Tech.*, vol. 39, pp. 1021–1025, June 1991.

[3] B. M. A. Rahman and J. B. Davies, "Finite-element analysis of optical and microwave problems," *IEEE Trans. Microwave Theory Tech.*, vol. MTT-32, pp. 531–541, May 1984.

[4] P. Savi, I.-L. Gheorma, and R. D. Graglia, "Full-wave high-order FEM model for lossy anisotropic waveguides," *IEEE Trans. Microwave Theory Tech.*, vol. 50, pp. 495–500, Feb. 2002.

[5] J. P. Webb, "Hierarchical vector basis functions of arbitrary order for triangular and tetrahedral elements," *IEEE Trans. Antennas Propagat.*, vol. 47, pp. 1244–1253, Aug. 1999.

[6] D.-K. Sun, J.-F. Lee, and Z. Cendes, "Construction of nearly orthogonal Nedelec bases for rapid convergence with multilevel preconditioned solvers," *SIAM J. Sci. Comput.*, vol. 23, no. 4, pp. 1053–1076, 2001.

[7] A. Bossavit and I. Mayergoyz, "Edge-elements for scattering problems," *IEEE Trans. Magn.*, vol. 25, pp. 2816–2821, July 1989.

[8] R. Albanese and G. Rubinacci, "Solution of three dimensional eddy current problems by integral and differential methods," *IEEE Trans. Magn.*, vol. 24, pp. 98–101, Jan. 1998.

[9] S. V. Polstyanko and J.-F. Lee, "$H_1(\mathrm{curl})$ tangential vector finite element method for modeling anisotropic optical fibers," *J. Lightwave Technol.*, vol. 13, pp. 2290–2295, Nov. 1995.

[10] S. V. Polstyanko, R. Dyczij-Edlinger, and J.-F. Lee, "Fast frequency sweep technique for the efficient analysis of dielectric waveguides," *IEEE Trans. Microwave Theory Tech.*, vol. 45, pp. 1118–1126, July 1997.

[11] R. Dyczij-Edlinger, G. Peng, and J.-F. Lee, "Efficient finite element solvers for the Maxwell equations in the frequency domain," *Comput. Methods Appl. Mech. Eng.*, vol. 169, no. 3–4, pp. 297–309, Feb. 1999.

[12] J. C. Nedelec, "Mixed finite elements in $\mathbb{R}^3$," *Nemer. Math.*, vol. 35, pp. 315–341, 1980.

[13] R. Albanese and G. Rubinacci, "Solution of three dimensional eddy current problems by integral and differential methods," *IEEE Trans. Magn.*, vol. 24, pp. 98–101, Jan. 1998.

[14] P. P. Silvester, "Universal finite element matrices for tetrahedral," *Int. J. Numer. Methods Eng.*, vol. 18, pp. 1055–1061, 1982.

[15] J.-F. Lee, "Finite element analysis of lossy dielectric waveguides," *IEEE Trans. Microwave Theory Tech.*, vol. 42, pp. 1025–1031, June 1994.

[16] S. V. Polstyanko, "Fast adaptive Schwarz-type finite element approach for solving electrostatic problems," Ph.D. dissertation, Dept. Elect. Comput. Eng., Worcester Polytech. Inst., Worcester, MA, 2000.

[17] J. V. Bladel, *Singular Electromagnetic Fields and Sources*. New York: Oxford Univ. Press, 1991.

Seung-Cheol Lee was born in Seoul, Korea, on August 4, 1974. He received the B.S. degree in electrical engineering from Hong-Ik University, Seoul, Korea, in 2000, and is currently working toward the M.S. degree in electrical engineering at The Ohio State University, Columbus.

He is currently with the ElectroScience Laboratory, Department of Electrical and Computer Engineering, The Ohio State University. His research focuses on numerical methods for waveguide, scattering, and radiation problems in electromagnetics.

Jin-Fa Lee (S'85–M'85) received the B.S. degree from the National Taiwan University, Taiwan, R.O.C., in 1982, and the M.S. and Ph.D. degrees from Carnegie-Mellon University, Pittsburgh, PA, in 1986 and 1989, respectively, all in electrical engineering.

From 1988 to 1990, he was with the Ansoft Corporation, where he developed several computer-aided design (CAD)/computer-aided engineering (CAE) finite-element programs for modeling three-dimensional microwave and millimeter-wave circuits. His doctoral studies resulted in the first commercial three-dimensional FEM package for modeling RF/microwave components, i.e., *HFSS*. From 1990 to 1991, he was a Post-Doctoral Fellow with the University of Illinois at Urbana-Champaign. From 1991 to 2000, he was with the Department of Electrical and Computer Engineering, Worcester Polytechnic Institute. He is currently an Associate Professor with the ElectroScience Laboratory, Dept. of Electrical Engineering, The Ohio State University, Columbus. His current research interests are analyses of numerical methods, fast finite-element methods, integral-equation methods, hybrid methods, three-dimensional mesh generation, and nonlinear optic fiber modelings.

Robert Lee (S'82–M'83–SM'01) received the B.S.E.E. degree from Lehigh University, Bethlehem, PA, in 1983, and the M.S.E.E. and Ph.D. degrees from the University of Arizona, Tucson, in 1988 and 1990, respectively.

From 1983 to 1984, he was a Microwave Engineer with the Microwave Semiconductor Corporation, Somerset, NJ. From 1984 to 1986, he was a Member of the Technical Staff with Hughes Aircraft Company, Tucson, AZ. From 1986 to 1990, he was a Research Assistant with the University of Arizona. In addition, during the summers of 1987–1989, he was with Sandia National Laboratories, Albuquerque, NM. Since 1990, he has been with the ElectroScience Laboratory, Department of Electrical and Computer Engineering, The Ohio State University, Columbus, where he is currently a Professor. His major research interests are in the development and application of numerical methods for electromagnetics.